The application of J integral to measure cohesive laws under large-scale yielding

Goutianos, Stergios; Sørensen, Bent F.

Published in:
Engineering Fracture Mechanics

Link to article, DOI:
10.1016/j.engfracmech.2016.01.004

Publication date:
2016

Document Version
Peer reviewed version

The Application of J Integral to Measure Cohesive Laws under Large-Scale Yielding

Stergios Goutianos, Bent F. Sørensen*

Department of Wind Energy, Section of Composites and Materials Mechanics, Technical University of Denmark, Risø Campus, DK-4000 Roskilde, Denmark

Abstract

A method is developed to obtain the mode I cohesive law of elastic-plastic materials using a Double Cantilever Beam sandwich specimen loaded with pure bending moments. The approach is based on the validity of the J integral for materials having a non-linear stress-strain relationship without unloading of any material point. This assumption is not met exactly as there is a small region at the active cohesive zone where the material unloads. To examine the error of the method, a numerical parameter study is performed for a wide range of material and specimen parameters. The error of the method is below 16% and thus the method can be used to measure cohesive laws including their shape.

Keywords: J Integral; Cohesive Law; Non-Linear Material, Plasticity

1. Introduction

Linear elastic fracture mechanics (LEFM) is applicable [1] when the fracture process zone is very small in comparison with all length dimensions (including the crack size) of a component. The fracture process zone is then embedded within a universal crack tip stress field (the so-called K-dominant zone). In contrast, when the size of the fracture process zone is comparable to or larger than any relevant specimen dimension, the fracture process zone should be modelled by non-linear fracture mechanics *e.g.* by a cohesive zone

*Corresponding author
Email address: bsqr@dtu.dk (Bent F. Sørensen)

model [2–7]; describing the fracture process of materials through a traction separation relationship as shown in Fig. 1.

Since Needleman [8] introduced a mode I cohesive law in a continuum mechanics finite element model, cohesive zone modelling has been widely used in advanced numerical models of materials and structures [9–15]. However, despite the widespread use of cohesive laws, the number of studies covering the experimental determination of cohesive laws is relatively small [16]. In most cases, the cohesive laws are determined indirectly by comparing experimentally measured specimen response (*e.g.* overall load-displacement relationships) with model predictions for a number of cohesive law parameters through an iterative guessing process [11, 17]. These approaches can be used for both elastic and elastic-plastic materials. The shortcomings of these approaches are a) that they usually require extensive computational effort to extract the cohesive law parameters (each specimen must be modelled when new experimental results are obtained), and b) that the shape of the cohesive laws is pre-defined and not an outcome from the experiments.

A small number of experimental methods have been developed to determine cohesive laws directly [6, 18, 19]. Cox and Marshall [6] back-calculated the cohesive tractions, σ, using fracture mechanics based on experimentally measured crack opening profiles. To obtain the full cohesive law, the crack opening profile should be measured at (stationary) cracks including cracks for which the end-opening is equal or larger than the critical separation, δ_c (Fig. 1). For most configurations, however, it is difficult to avoid crack growth, unless the specimen is partially unloaded. However, unloading alters the cohesive tractions so they differ from the tractions acting in the cohesive zone during monotonic loading. Cotterell and Mai [18] and Brenet et al. [19] used the so-called direct tension test. Calculating the traction as the force per cross-sectionnal area and measuring the displacement between two points across the cohesive/failure plane with an extensometer, the cohesive law can be measured. However, the separation is not always uniform across the width of the specimen. Thus, these experimental techniques are either involved and/or it is difficult to achieve the correct conditions [16]. An alternative method is to derive the cohesive law from measurements of the path independent J integral [20] and the end-opening of the cohesive zone as proposed by Li and Ward [21]:

$$\sigma = \frac{dJ}{d\delta^*} \tag{1}$$

where J is the value of the J integral [20] and δ^* is the end-opening, *i.e.* the crack opening displacement at the end of the fracture process zone. It should be noted that the J integral approach is valid also for problems involving large-scale bridging (large fracture process zone) [7, 22].

Li and Ward [21] used two different compact tension specimens to determine the J integral. Sørensen and Jacobsen [23] also used the J integral approach, Eq. 1, but they used a single double cantilever beam (DCB) specimen loaded with pure bending moments. In this case the J integral can be derived in closed form [7], and the mode I bridging/cohesive law can be directly measured using Eq. 1. A closed form solution exists also for other DCB specimen loaded by axial forces and bending moments such as a bimaterial/sandwich DCB specimen (see Fig. 2) when both materials are linear elastic [24]. For linear elastic materials, the J integral value increases to a maximum value when the end-opening attains the critical separation, δ_c, and J remains at this steady-state value, J_{ss}, during subsequent crack propagation. A differentiation of J according to Eq. 1 gives - correctly - zero traction for $\delta^* > \delta_c$.

In the works described above, the material outside the fracture process zone was assumed to be elastic. However, many materials *e.g.* polymers or composites have a non-linear stress-strain relation that needs to be taken into account.

The study of Tvergaard and Hutchinson [9] gives insight into the roles of cohesive law and plasticity on the overall fracture resistance. They modeled crack propagation under the premise of small scale yielding using a cohesive law and a bulk material exhibiting plasticity embedded in a K-field. Despite the formation of a plastic zone at the cohesive zone, the initiation of crack growth (δ^* reaching δ_c) was found to occur at $J = J_c$. This result was anticipated since - during monotonic loading prior to crack growth - the stresses increase nearly proportionally and the conditions for applicability of a deformation theory [25] are thus met. The application of the J integral for materials having non-linear stress-strain relationship is valid as long there is no unloading of any material point so that the non-linear stress-strain behaviour can then be considered as being non-linear elastic [20] (*a.k.a.* deformation theory) [25]. In the simulation of Tvergaard and Hutchinson [9], once crack propagation occured, the fracture resistance increased since now unloading (non-proportional stress history) took place. Eventually, after some crack propagation, the fracture resistance attained a constant, steady-state value. According to Tvergaard and Hutchinson [9] the value of the steady-state frac-

ture resistance depends strongly on the ratio of the peak cohesive traction value $\hat{\sigma}$ to the yield stress, σ_y, of the bulk material. J_{ss}/J_c was found to be in the range of 2-10 for $\hat{\sigma}/\sigma_y$ in the range of 3-4.

Thus, in the case of crack growth with plastic unloading, a differentation of the fracture resistance according to Eq. 1 would not give zero traction for $\delta^* > \delta_c$. This makes it difficult to determine cohesive laws for elastic-plastic materials by the J integral approach, Eq. 1. Thus, so far, in the previous studies involving large scale plasticity, cohesive laws have been identified by the iterative guessing approach described above [11, 12, 17].

The idea of the present study is to explore whether it is possible to design fracture specimens for materials that exhibit large scale yielding during fracture. This will be possible if the specimens undergo only a rather small unloading during crack propagation. Then, the fracture resistance, calculated using the J integral, will not show a significant increase due to the plastic unloading but retain a steady-state value, J_{ss}, close to the work of separation per unit area of the cohesive law, J_c. The cohesive law can then be determined using Eq. 1, - and correctly give zero cohesive traction for end-openings exceeding δ_c despite the occurrence of large scale plasticity. From an experimental point of view this would greatly simplify the cohesive law determination and enable a general approach for cohesive law determination also for non-linear elastic materials.

The proposed specimen configuration is a sandwich specimen, consisting of stiff elastic beams bonded to the non-linear test material, loaded with pure bending moments. The use of the additional elastic beams in sandwich specimens can be a practical issue; *i.e.* to prevent large rotation of the specimen which adds complexity to the analytical approach [26]. Moreover, the use of stiff elastic beams facilitates the mounting of the specimen to the fixture avoiding local failure at the point of fixation.

Thus, in the present work, inspired by the work of Thouless et al. [27], who used the I integral [28] for the analysis of steady-state cracking involving large-scale plasticity, the general J integral based testing approach using DCB specimens loaded by pure bending moments is extended to account for the non-linear material response (*e.g.* due to plasticity). Fig. 2 shows the proposed DCB sandwich specimen loaded with pure bending moments. During loading, plasticity may occur in the beams made of the test material (but not in the stiff, elastic support beams), but since the value of the moment must be increased during the experiment to increase J, there will be no unloading in the beams for the DCB specimen loaded with pure bending

moments. In contrast, the standard DCB specimen loaded with wedge forces is not suited for large scale yielding problems since the magnitude of the force decreases during stable crack growth *i.e.* the specimen unloads causing unloading in materials points having undergone plastic deformation which invalidates the use of the J integral.

For the DCB specimen loaded with pure bending moments, an equation for the J integral can be obtained analytically if the stress-strain law of the test material is known (see Section 2.1). The equation for the J integral is independent of the crack length and the details of the cohesive zone. Even when the crack starts to grow there is no macroscopic unloading in the plastically deforming beams. However, there is a small region behind the active crack tip *e.g.* in the case of plasticity, where unloading takes place. Thus, the proposed method is expected to introduce an error in evaluating the J integral and consequently an error in the derived cohesive laws. The aim of the present study is to explore if the J integral approach (Eq. 1) can also be used to determine cohesive laws under large scale plasticity and to estimate how large the error can be.

In the present paper, a parameter study is performed to evaluate this error for a wide range of material and geometric parameters, in order to clarify if this error is large *e.g.* in comparison with the scatter of typical experimental fracture mechanical testing results. The error of the method is estimated by finite element predictions. More specifically, we use the finite element method to generate simultaneous data for the applied moments and the end-opening and then use the moments in the analytical model (as if the data were experimental measurements) to calculate J as a function of δ^*. Then by Eq. 1, we calculate the cohesive law, which we can then compare with the cohesive law specified in the finite element model.

2. Problem statement

The specimen geometry used is a double cantilever beam (DCB) sandwich specimen loaded with pure bending moments [16, 29] (see Figs. 2 and 3). The non-linear test material (material #2) is fixed to stiff elastic beams (material #1). The thickness of the non-linear material is $2h$, whereas the thickness of each elastic beam is H. The specimen and loading are symmetric, and the crack is assumed to propagate along the specimen mid-plane (mode I).

The fracture process is represented by a trapezoidal shaped cohesive law as shown in Fig. 1, and the material #2 has a non-linear stress-strain law

(representing plasticity), so that plasticity may form at the crack tip and in the beams (large scale yielding). The non-linear stress-strain behaviour will be described using a specific formulation that enables the J integral analysis to be completed analytically (see below).

2.1. Stress-strain laws

Material #1 is taken to be linear elastic, so that $\sigma_{11}^{\#1}$, the stress component acting in the x_1 direction of material #1 is related to the normal strain ϵ_{11} via Hooke's law:

$$\sigma_{11}^{\#1} = E^{\#1}\epsilon_{11} \tag{2}$$

where $E^{\#1}$ is the Young's modulus of material #1.

For the analytical J integral analysis material #2 is assumed to be non-linear elastic:

$$\sigma_{11}^{\#2} = f(\epsilon_{11}) = E^{\#2}\epsilon_{11} - \sigma_o\epsilon_{11}^2 \tag{3}$$

where $E^{\#2}$ is the Young's modulus and σ_o a constant. Thus in the limit of $\epsilon_{11} \to 0$, the slope of the stress-strain curve is $E^{\#2}$. Both $E^{\#2}$ and σ_o are determined by fitting Eq. 3 to the experimental stress-strain response. The particular form of the function $f(\epsilon_{11})$ is material dependent. Eq. 3 was found to describe the tensile stress-strain behaviour of all-cellulose composites rather well [30] and is used in the present work as an example; however, the approach can be extended to other constitutive laws than Eq. 3. In Eq. 3 no distinction is made if the response is non-linear elastic or elastic-plastic. For example, Fig. 4 depicts the tensile stress-strain behaviour of an elastic-plastic material. As long there is no unloading, the stress-strain response can be described by a monotonically increasing function $f(\epsilon_{11})$. It should be noted that Eq. 3 is a parabolic equation *i.e.* the stress decreases after a characteristic strain, ϵ_u, has been reached. The maximum stress, σ_u, is given by:

$$\sigma_u = \frac{E^{\#2^2}}{4\sigma_o} \text{ and } \epsilon_u = \frac{E^{\#2}}{4\sigma_o} \tag{4}$$

In the remainder of the paper, we will present results expressed through σ_o or σ_u whenever we find most appropriate. For $\epsilon_{11} > \epsilon_u$, Eq. 3 is not valid *i.e.* the normal stress in the beam ends made of the tested material should not exceed σ_u. Alternatively, a second function *i.e.* a constant function,

$\sigma_{11}^{\#2} = \sigma_u$, could be used for strains larger than ϵ_u. In the present work, this was not necessary.

As shown below, in Section 3.2, only the normal stress in the direction parallel to the specimen is needed to calculate the J integral along the external boundaries of the specimen. Thus, it is not necessary to derive a complete constitutive material law from the experimenal data; a one-dimensional material description as in Eq. 3 suffices.

For the finite element (FE) simulations, material #2 is described with an elastic-plastic stress-strain law that has an initial yield stress σ_y. When the sandwich DCB specimen (Fig. 2) is modelled with the finite element method (multiaxial stress state), the one-dimensional Eq. 3 is not enough. A complete material constitutive law should be used. In the present work, material #2 is modelled as an elastic-plastic material governed by the von Mises J_2 plasticity theory with isotropic hardening: the von Mises stress is $\sigma_e = \sqrt{3S_{ij}S_{ij}/2}$ where S_{ij} are the deviatoric stresses. The initial yield stress is denoted σ_y and it is shown in Fig. 4. In the same figure the unloading/reloading response in the finite element model is also shown. The plastic response used in the finite element model was extracted from Eq. 3 with the following two differences: a) for stresses lower than σ_y the material is linear elastic with a Young's modulus $\tilde{E}^{\#2}$, and b) for strains larger than ϵ_u, an ideal plastic response is assumed (see Fig. 4). In Fig. 4 the difference between the stress-strain relationship of Eq. 3) and of the FE model for $\sigma < \sigma_y$ is exaggerated. In practise the difference between $E^{\#2}$ and $\tilde{E}^{\#2}$ is less than 5%.

It should be noted, that although the normal strains in the beam ends for the test material are lower than ϵ_u, much higher strains are expected in the vicinity of the fracture process zone. By assuming an ideal-plastic response for $\epsilon > \epsilon_u$, the finite element model can handle such large strains. The assumption of ideal-plastic response is a simple approximation but it approximates the plastic response of many materials for fairly large strains.

2.2. Cohesive law

The cohesive law parameters used in the finite element model define a trapezoidal shaped cohesive law shown in Fig. 1. The area under the curve is the work of separation per unit area, J_c. The peak traction $\hat{\sigma}$ is attained at an opening δ_1, and the opening at complete failure is δ_c. The opening δ_2 completes the description of the trapezoidal cohesive law. Four out of the

five cohesive law parameters are independent. In the following, we take $\hat{\sigma}$, δ_1, δ_2, and δ_c as the primary parameters.

$$\sigma(\delta) = \begin{cases} \hat{\sigma}\dfrac{\delta}{\delta_1}, & \text{for } 0 \leq \delta < \delta_1, \\ \hat{\sigma}, & \text{for } \delta_1 \leq \delta < \delta_2, \\ \hat{\sigma}\Big(\dfrac{\delta_c - \delta}{\delta_c - \delta_2}\Big), & \text{for } \delta_2 \leq \delta \leq \delta_c, \\ 0, & \text{for } \delta > \delta_c, \end{cases} \tag{5}$$

J_c can be expressed by these parameters, see Section 3.3.

2.3. Non-dimensional parameters

A parameter study is performed in this paper to assess the effect of the various parameters in the fracture resistance and consequently on the computed cohesive laws. The non-dimensional parameters describing the problem of Fig. 2 are:

$$\frac{\delta_1}{h}, \quad \frac{\delta_2}{\delta_c}, \quad \frac{\delta_c}{h}, \quad \frac{E^{\#2}}{E^{\#1}}, \quad \frac{\hat{\sigma}}{\sigma_u}, \quad \frac{\hat{\sigma}}{E^{\#2}}, \quad \frac{\sigma_u}{E^{\#2}}, \quad \frac{h}{H} \tag{6}$$

Some of these parameters were kept constant in all simulations, $\delta_1/h = 2 \times 10^{-4}$ and $h/H = 1$ (except Section 5.4). The critical opening for damage initiation, δ_1, is non-zero in the finite element calculations purely for numerical reasons.

The additional parameters needed in the finite element model are the initial yield stress, σ_y, which is set as a fraction of the Young's modulus $E^{\#2}$:

$$\frac{\sigma_y}{E^{\#2}} = 0.01 \tag{7}$$

and the Young's modulus $\tilde{E}^{\#2}$ which is calculated from Eq. 3 at $\sigma_{11}^{\#2} = \sigma_y$ giving:

$$\tilde{E}^{\#2} = \frac{E_2^{\#2}}{2\sigma_u} \quad \frac{\sigma_y}{1 - \sqrt{1 - \sigma_y/\sigma_u}} \tag{8}$$

3. *J* integral approach for determination of cohesive laws

3.1. Stress state in the beam ends

In this paper, J will be expressed in terms of $\hat{\epsilon}$, which is the maximum strain in the top of the stiff, elastic beam, see Fig. 5. In the following, $\hat{\epsilon}$ is determined as a function of the applied moment, $\hat{\epsilon} = \hat{\epsilon}(M)$. Since the beam-ends are subjected to pure bending, the strain varies linearly across the height of the specimen (due to symmetry only the upper half of the specimen is considered):

$$\epsilon_{11} = \frac{\hat{\epsilon}}{\Delta} y, \text{ for } \Delta - H - h \leq y < \Delta \tag{9}$$

where y is the distance from the neutral axis in a local coordinate system with origin the neutral axis as can be seen in Fig. 5. The relationship between this local coordinate system, $x-y$, and the global coordinate system, x_1-x_2, defined in Fig. 5, is:

$$y = x_2 + \Delta - H - h \tag{10}$$

The neutral axis position (the distance from the top of the elastic beam to the y position where $\epsilon_{11} = 0$ under pure bending), Δ, is given by:

$$\frac{\Delta}{h} = \frac{1 + 2\bar{\Sigma}\eta + \bar{\Sigma}\eta^2}{2\eta(\bar{\Sigma}\eta + 1)} \tag{11}$$

where the non-dimensional constants η and $\bar{\Sigma}$ (for plane stress), which depend on the elastic properties and the geometry of the specimen, are:

$$\eta = \frac{h}{H} \tag{12}$$

and

$$\bar{\Sigma} = \frac{E^{\#2}}{E^{\#1}} \tag{13}$$

Eq. 11 is based on linear elasticity [24]. For the present problem, the neutral axis may change position as the plasticity changes the stress distribution. In the following, however, we assume that the change is small such that the neutral axis position can be approximated by Eq. 11. With this assumption, a closed form solution for the J integral along the external boundaries of the DCB specimen can be obtained. In Appendix A the change in position of

the neutral axis is calculated analytically (accounting for the non-linearity of material #2) and it is shown that the change in Δ is smaller than 1.5% in the range of parameters examined in the present work.

The applied moment, M, is then given by:

$$\frac{M}{B} = \int_{\Delta-H-h}^{\Delta-H} \sigma_{11}^{\#2}(y) y dy + \int_{\Delta-H}^{\Delta} \sigma_{11}^{\#1}(y) y dy \tag{14}$$

where B is the specimen width (in x_3 direction). The first integral refers to the non-linear material and the second integral to the elastic beam. By substituting the stress in the non-linear material with Eq. 3 and Eq. 9, Eq. 14 can be written as:

$$A\hat{\epsilon}^2 + C\hat{\epsilon} + D(M) = 0. \tag{15}$$

Solving Eq. 15 gives:

$$\hat{\epsilon} = g(M) = \frac{-C \pm \sqrt{C^2 - 4AD(M)}}{2A}, \tag{16}$$

where $D(M)$ indicates that D is a function of the applied moment:

$$D = -\frac{M}{BH^2 E^{\#1}} \tag{17}$$

In Eq. 16 the positive sign ahead of the square root is selected to ensure that for $M = 0$, $\hat{\epsilon} = 0$ and an increase of M results in an increase of $\hat{\epsilon}$. The other non-dimensional parameters A and C are independent of M:

$$A = \frac{{E^{\#2}}^2}{16\Delta^2 H^2 E^{\#1} \sigma_u} \Big[(\Delta - H)^4 - (\Delta - H - h)^4 \Big] \tag{18}$$

$$C = \frac{E^{\#2}}{3\Delta H^2 E^{\#1}} \Big[(\Delta - H)^3 - (\Delta - H - h)^3 \Big] + \frac{1}{3\Delta H^2} \Big[\Delta^3 - (\Delta - H)^3 \Big] \tag{19}$$

From Eq. 16, $\hat{\epsilon}$ can be obtained analytically as a function of M. For different functions $f(\epsilon_{11})$ it may not be possible to obtain a closed form solution. In such cases, Eq. 14 can be solved numerically. In Appendix B, closed form solutions for homogeneous DCB specimens are given for two different stress-strain relationships: a) power law, and b) elastic-ideal plastic, respectively.

3.2. J integral evaluated along the external boundaries, J_{ext}

The J integral is calculated along a path along the external boundaries of the specimen Γ_i with $i = 1, 5$ shown in Fig. 3. If the beams outside the fracture process zone are longer than a few times the specimen (beam) height, the J integral is independent of the crack length. This holds true since the only non-zero contributions to the J integral come from the two loaded beam ends, which are subjected to pure bending. The only stress component that enters the analysis is the normal stress in the direction parallel to the crack, σ_{11} (the x_1 direction in Fig. 3), *i.e.* along Γ_1 and Γ_5.

The J integral is defined as [20]:

$$J = \int_{\Gamma} \Phi dx_2 + \sigma_{ij} n_j \frac{\partial u_i}{\partial x_1} dS \tag{20}$$

where Φ is the strain energy density, σ_{ij} the stress tensor, u_i the displacement vector, n_j is the outward normal unit vector to the integration path Γ which should be evaluated in counter clockwise direction. Then, the J integral along path Γ_5 can be written as:

$$J_5 = \int_{H+h}^{h} (\Phi^{\#1} - \sigma_{11}^{\#1} \epsilon_{11}) dx_2 + \int_{h}^{0} (\Phi^{\#2} - \sigma_{11}^{\#2} \epsilon_{11}) dx_2 \tag{21}$$

In this Equation the strain energy density function, $\Phi^{\#1}$, for material #1 (linear elastic) is:

$$\Phi^{\#1} = \frac{{\sigma_{11}^{\#1}}^2}{2E^{\#1}} = \frac{1}{2} E^{\#1} \epsilon_{11}^2 \tag{22}$$

whereas for the non-linear material #2, the strain energy density function, $\Phi^{\#2}$, using Eq. 3, is:

$$\Phi^{\#2} = \int_0^{\epsilon_{11}} \sigma_{11}^{\#2} d\epsilon_{11} = \frac{E^{\#2} \epsilon_{11}^2}{2} - \frac{E^{\#2} \epsilon_{11}^3}{12 \sigma_u} \tag{23}$$

Using Eqs. 3, 9, 22, 23, Eq. 21 becomes:

$$J_5 = \frac{E^{\#1}\hat{\epsilon}^2}{2\Delta^2}\left(\Delta^2 H - \Delta H^2 + \frac{H^3}{3}\right) + \frac{E^{\#2}\hat{\epsilon}^2}{2\Delta^2}\left(\frac{h^3}{3} + h^2(\Delta - H - h) + h(\Delta - H - h)^2\right) + \frac{E^{\#2^2}\hat{\epsilon}^3}{6\sigma_u\Delta^3}\left(\frac{h^4}{4} + h^3(\Delta - H - h) + \frac{3h^2}{2}(\Delta - H - h)^2 + h(\Delta - H - h)^3\right) \quad (24)$$

The J integral along the external boundaries for the DCB specimen (Fig. 3) is thus due to symmetry:

$$J_{ext} = 2J_5. \quad (25)$$

3.3. J integral evaluated around the cohesive zone, J_{loc}

Next, the J integral is considered along an integration path locally around the fracture process zone. In this case the J integral given by [7, 20]:

$$J_{loc} = \int_0^{\delta^*} \sigma(\delta) d\delta \quad (26)$$

where δ^* is the normal opening at the end of the fracture process zone. Differentation of Eq. 26 gives Eq. 1. When $\delta^* = \delta_c$, J_{loc} is equal to J_c:

$$J_c = \int_0^{\delta_c} \sigma(\delta) d\delta = \frac{1}{2}\hat{\sigma}(\delta_c + \delta_2 - \delta_1) \quad (27)$$

Since the J integral is path independent and as long as there is no unloading, J_{loc} from Eq. 27 equals J_{ext} from Eq. 25. Thus, by measuring the applied moment and normal opening at the end of the cohesive zone (fracture process zone), the cohesive laws including their shape can be derived experimentally.

4. Numerical model

In order to test the accuracy of the J integral approach presented in Section 3, the finite element method was employed to model the DCB specimen of Fig. 2 as a 2D plane stress problem. The commercial finite element code Abaqus (version 6.11) [31] was used. Cohesive elements were used to model crack initiation and growth.

4.1. Finite element details

The length of the DCB specimen, L, was long enough ($L/h = 24$) to ensure that when steady-state condition is reached, the position of the crack tip is several times the specimen height far away from the right end of the specimen (Fig. 2). In the following, the position of the crack-tip is defined as the position within the active cohesive zone where the end-opening δ^* equals δ_c, *i.e.* where the cohesive traction decreases to zero (see Fig. 1) [9].

The initial crack-tip position was set to be at $8h$ from the position where the applied moments were applied (Fig. 2). The position of the initial crack-tip coincides with the origin of the $x_1 - x_2$ coordinate system of Fig. 3. In the finite element model, applied rotations were prescribed at the beam ends (as would be the case experimentally) and the resulting reaction moments were extracted.

An implicit solver was used to solve the problem of Fig. 3 under plane stress conditions. Four-noded quadrilateral and three-noded triangular linear, full-integration elements were used to model the linear and non-linear materials. The Abaqus linear four-noded cohesive elements were used to model the cohesive zone and the cohesive element length was equal to $5 \times 10^{-3}h$. The finite element mesh was deemed to be sufficiently fine, since the correct fracture resistance and cohesive law were obtained in the case of vanishing plasticity (see below). The numner of elements in the cohesive zone was larger than the size suggested by Turon et al. [32] and references therein for elastic-plastic materials.

4.2. Method to check the J integral approach

The end-opening, δ^*, and the applied moment, M, were extracted from the finite element model. Then, from the applied moment, the fracture resistance, J, was calculated using the analytical stress-strain law, Eq. 3, following the approach of Section 3 (J is given in terms of $\hat{\epsilon}$ by Eqs. 24 and 25 and $\hat{\epsilon}$ is obtained from M through Eqs. 16 - 19). With J and δ^* known, the cohesive law was derived using Eq. 1. The differentiation of the $J - \delta^*$ was done directly on the data and not on a fitted curve using the following simple equation:

$$\sigma_i = \frac{J_i - J_{i-i}}{\delta_i^* - \delta_{i-1}^*} \tag{28}$$

where i represents the increment in applied moment. This direct differentiation method inherently introduces noise to the predicted cohesive laws

but it is chosen here because it does not manipulate the data in any form (*e.g.* smoothing or filtering).

The obtained cohesive law is then compared with the cohesive law originally specified in the finite element model. If the effect of plasticity and local unloading is small, the two cohesive laws will be very similar.

5. Results

Fig. 6 shows the development of the plastic zone in the DCB specimen as a function of the end-opening, δ^*. In Fig. 6(a), the stress normal to the crack plane has already reached the peak cohesive value, but the cohesive zone is not fully developed. Next in Fig. 6(b) the end-opening is equal to $\delta_c/2$ and J is $\sim 80\%$ of J_c. A large plastic zone has developed ahead of the crack tip due to the stresses normal to the crack plane, and a plastic zone has formed in the beam behind the crack due to the bending of the DCB specimen (stresses parallel to the crack plane). The plastic zone ahead of the crack tip has reached the interface between materials #1 and #2 ($x_2 = \pm h$). In Fig. 6(c), where δ^* equals δ_c, the plastic zone ahead of the crack tip has extended in both the x_1 and x_2 directions. A further increase of the plastic zone can be seen in Fig. 6(d) where the $\delta^* \sim 1.4\ \delta_c$. At this instance the crack has grown a distance $\Delta a = 0.1h$.

Fig. 7 shows the corresponding active plastic zone (currently yielding material points) contours of the equivalent plastic strain contours of Fig. 6. Fig. 7(a) shows the active plastic zone at an instance where the cohesive zone is not fully developed ($\delta_1 < \delta^* < \delta_c$ and $J = 0.25J_c$). The active plastic zone is confined around the crack tip and behind the cohesive zone at $x_2 = 0$. With further increase of the applied moment, see Fig. 7(b), the yielding zone extends both ahead and behind the crack tip (crack wake). Almost all the material points of the non-linear material #2 are yielding except the materials points that are far ahead from the crack tip. When δ^* reaches δ_c (see Fig. 7(c)), unloading takes place at a small region behind the crack tip corresponding approximately to the length of the fully developed cohesive zone. However, no unloading is observed in the materials points that are subjected to bending - behind the fracture process zone. Furthermore, the active plastic zone size increases ahead of the crack tip. In Fig. 7(d) the crack has grown at a distance equal to $0.1h$ ($\delta^* = 1.4\delta_c$). It can be seen that although the unloading zone has grown, it is confined between two zones where the materials points are currently yielding: a zone ahead of the crack

tip, which is increased in size comparable to the corresponding zone shown in Fig. 7(c) and a zone behind the fracture process zone where the is no unloading of the material points due to bending of the beams of material #2.

5.1. Derivation of cohesive laws

Fig. 8 depicts the applied moment *vs* the end-opening extracted directly from the finite element calculations for three different cohesive laws. The peak cohesive traction, $\hat{\sigma}$, and the opening δ_c are the same, whereas the opening δ_2 and thus the work of separation, J_c, differ for each cohesive law in accordance with Eq. 27. The fracture resistances, calculated from the moments, are depicted (solid lines) as function of the end-opening in Fig. 9. The dotted lines in Fig. 9 represent the fracture resistance curves obtained by analytical integration of the corresponding cohesive laws according to Eq. 26, *i.e.* the theoretically correct work of the cohesive traction. It can be seen that the steady-state fracture resistance, J_{ss} for each cohesive law is slightly higher than the corresponding work of separation, J_c, and that the steady-state is attained at an end-opening larger than δ_c. As mentioned in Section 1, a higher J_{ss} is expected as there is a region where the material unloads behind the crack tip (see Fig. 7). The difference in the steady-state fracture resistance is less than 10% for the three cohesive laws.

The cohesive laws extracted from the data of Fig. 9 are given in Fig. 10. The extracted cohesive laws are shown with solid lines, whereas the dashed lines represent the cohesive laws originally specified in the finite element model. Despite the noise, the extracted cohesive laws agree well with the specified cohesive laws. In particular, the extracted cohesive laws capture the shape of the input cohesive laws well. For the examples shown, the values of δ_2 and δ_c can readilly be identified. The extracted peak traction is slightly higher than the specified parameter. This is a direct result of a higher computed fracture resistance (Fig. 9). However, similar to the results of Fig. 9, the difference between the extracted and specified cohesive law parameters is less than 10%.

The difference between the obtained fracture resistance curves and the expected curves increases with increasing end-opening. It is interesting to observe (Fig. 9) that as δ_2/δ_c increases, the difference decreases.

In the next Sections, the results are presented for J_{ss} (and not for $\sigma - \delta$), since it is expected that when $J_{ss} \approx J_c$, the computed cohesive law will be similar to the specified.

5.2. Effect of cohesive law parameters

In this Section the effect of the cohesive law parameters is examined. The elastic-plastic stress-strain relationship for material #2 and the geometry of the DCB specimen are kept constant.

Fig. 11 shows the effect of the opening δ_2 (see Fig. 1) on the steady-state fracture resistance for different ratios between the peak cohesive traction, $\hat{\sigma}$, and σ_u. As it can be seen, for $\hat{\sigma}/\sigma_u < 1$, the steady-state fracture resistance is only slightly larger than J_c. The difference between J_{ss} and J_c is less than 15%. The difference decreases as the opening δ_2 increases relatively to δ_c. It should be noted that for constant δ_c, J_c increases as δ_2 increases, see Eq. 27. A larger value of δ_2 results in a larger region where the traction in the cohesive zone is equal to peak traction $\hat{\sigma}$. Furthermore, a larger value of δ_2 means a smaller region where the traction in the cohesive zone gradually reduces to zero, leading to a smaller unloading region along the active cohesive zone.

J_{ss} increases sharply for $\hat{\sigma}/\sigma_u \cong 1.0 - 1.1$ ($\hat{\sigma}/\sigma_y \geq 5$) due to formation of a much larger plastic zone. For $\hat{\sigma}/\sigma_u \geq 1.2$ the material yields and no crack growth takes place ($J_{ss} \to \infty$). These results are in qualitative agreement with the results of Tvergaard and Hutchinson [9] who used a elastic-plastic stress-strain relationship different from the one used in the present paper.

In Fig. 11 the dotted line represents the linearly extrapolated steady-state fracture resistance in the absence of plasticity ($\hat{\sigma}/\sigma_u \to 0$). In this case the steady-state fracture resistance, J_{ss} is equal to J_c.

Fig. 12 depicts the extracted cohesive laws for large values of $\hat{\sigma}/\sigma_u$. It can be seen that for the same end-opening, δ^*, the extracted tractions are larger than the specified traction and that the difference increases with increasing $\hat{\sigma}/\sigma_u$. For $\delta^* > \delta_c$, the derived tractions do not drop to zero. This is especially clear for $\hat{\sigma}/\sigma_u = 1.2$.

In the results presented in the rest of the paper, the maximum value of $\hat{\sigma}$ considered is σ_u.

Next in Fig. 13, the effect of the critical opening δ_c relative to the height h is examined. For a fixed value of $\hat{\sigma}/\sigma_u$, a higher value of δ_c/h leads to a higher J_{ss} value. Futhermore, a larger value of δ_c/h gives a larger active cohesive zone size. As a result, when δ_c increases, the extend of the plastic zone increases and thus the size of the unloading region becomes larger.

5.3. Effect of elastic-plastic stress-strain law

The effect of the material parameters of the non-linear test material on the steady-state fracture resistance is examined in this Section. First, the

effect of the magnitude of the Young's modulus, $E^{\#2}$, relative to $E^{\#1}$ is investigated. Fig. 14 shows stress-strain curves, Eq. 3, with varying $E^{\#2}$. For all four curves, the ratio $E^{\#2}/\sigma_o$ is constant and equal to 0.2.

Steady-state fracture resistance results are given in Fig. 15. With other parameters fixed, an increase in $E^{\#2}/E^{\#1}$ increases J_{ss}, but the effect is small. It can be seen that, for the range of $E^{\#2}$ examined, the difference between J_{ss} and J_c is small (less than 15%) except the case of $E^{\#2}/E^{\#1} = 0.1$ and for $\hat{\sigma}/\sigma_u = 1$. For this case the difference is 16%.

Next in Figs. 16 and 17 the effect of varying σ_o is examined. However, in order to have the same plateau stress, σ_u, in the stress-strain response it is necessary to change $E^{\#2}$ at the same time, see Fig. 16. The strain at which the non-linear material #2 becomes fully-plastic ranges from 5 to 20%. The results for the steady-state fracture resistance are given in Fig. 17. It is interesting to observe that the difference between the steady-state fracture resistance, J_{ss} and J_c decreases with increasing σ_o. The difference is less than 15% in all cases except for the case of $E^{\#2}/E^{\#2} = 0.02$ and $\hat{\sigma}/\sigma_o = 1$.

In the same graph, the dashed lines represent the steady-state fracture resistance calculated from Eq. 25 by setting σ_o equal to zero (corresponding to $\sigma_u \to \infty$) in Eq. 24. This is equivalent to ignoring the non-linearity of material #2 in the analytical calculation of J. In this case Eq. 24 is identical to the closed form solution of Bao et al. [24]. Thus, by setting $\sigma_o = 0$ in the analytical model, the effect of not taking the non-linearity of material #2 into account can be assessed. As expected, when σ_o is set equal to zero, the difference between J_{ss} and J_c is higher than when the material non-linearity is taken into account (solid lines) for all $\hat{\sigma}$ values. The difference is larger for larger values of $\hat{\sigma}$. However, the difference in J_{ss} between $\sigma_o = 0$ and $\sigma_o \neq 0$ is relatively small.

5.4. Effect of DCB geometry

In the results presented above, the geometry of the DCB specimen was constant with $h = H$. Fig. 18 shows the difference between the steady-state fracture resistance, J_{ss} and J_c for different h/H values as a function of $\hat{\sigma}$. It is seen that the difference between J_{ss} and J_c increases when the beam thickness of the non-linear material increases relatively to the beam thickness of the stiff, linear elastic material. However, the effect is relative small (less than 15%). As a practical guidance, h can be decreased for materials where $\hat{\sigma} \approx \sigma_u$ in order to reduce the difference between J_{ss} and J_c. The effect of

decreasing J_{ss} with decreasing thickness of a plastic layer was also noted by Tvergaard and Hutchinson [33].

6. Discussion

6.1. Assessment of proposed method

The use of the J integral to describe the fracture resistance during crack growth with plastic unloading is not theoretical sound as pointed out by Hutchinson [34]. A more rigorous correct analysis involving energy accounting for both the cohesive zone and the bulk plasticity under steady-state could be made by the use of the I integral [34, 35]. However, from an engineering point of view, the approach proposed here may still be useful, when used in a proper context, since the J integral attains a steady-state value that in most cases examined is less than 15% of J_c. In practise this opens the possibility of determining cohesive laws using the J integral approach (Eq. 1) with fairly high accuracy.

Tvergaard and Hutchinson [9] found that for small scale yielding (plasticity occuring within a K-dominated region), the toughening due to plastic unloading could be more than 500% higher than J_c for $\hat{\sigma}/\sigma_y$ in the range of 3-4. The results of the current work, using a different plasticity law, show that for the proposed specimen that exhibits large scale yielding without significant unloading, the J integral attains a steady-state value that is less than 15% higher than J_c for $\hat{\sigma}/\sigma_u \leq 1$ ($\hat{\sigma}/\sigma_y = 5$). This is a quite remarkable feature of the proposed specimen and it is mainly due to the stiff, elastic beams attached to the non-linear material preventing significant unloading as shown below.

Examining the terms in Eq. 24, we note that the stiff, elastic beam actually gives a contribution that is significantly larger than that of the test material that deforms plastically. Although Eq. 24 does not account for the crack tip plasticity, it suggests that the presence of the stiff layer helps reducing the amount of crack tip plasticity and unloading. For instance, in comparison with a specimen without a stiff, elastic beam, the strain ϵ_{11} which - due to compatibility in displacements - must approximately follow the strain variation of Eq. 9, so that it is likely to be smaller in a specimen with a stiff beam and thus the amount of plastic deformation will be smaller. This hypothesis is consistent with the findings of Tvergaard and Hutchinson [33].

Fig. 19 shows schematically a material point in the non-linear material that is far-ahead from the initial notch. Upon loading of the DCB specimen,

crack growth takes place and the active cohesive law approaches the material point. With further increasing the applied moment, the active cohesive zone moves past the material point (or equivalently, as shown in Fig. 19, a material point moving past the active cohesive zone). Thus, by examining the stress history in the material point as the active cohesive zone moves past, the unloading can be examined. Fig. 20 shows the stress component σ_{11} in material points that are located at $x_1 = 0.08h$ *i.e.* ahead of the crack tip (the position of the initial crack tip is $x_1 = 0$) and different distances from the crack line in x_2 direction. Significant unloading takes place in the material points that are less than $0.03h$ far from the crack line as the crack tip passes by. However, for $x_2 > 0.045h$ there is almost no unloading of the material points. Fig. 21 shows the corresponding stress component σ_{22} for the same material points. As can be seen, σ_{22} decreases for all material points when they move behind the crack tip, irrespective of their distance to the crack plane ($x_2 = 0$). Behind the active cohesive zone, the beams of the non-linear material are subjected to nearly pure bending induced by the stiff, elastic beams. The elastic beams are loaded in pure bending without unloading.

As mentioned in Section 3, the present analytical solution is based on the assumption that the neutral axis of the DCB speciment does not move with the development of plasticity. In Appendix A a method is presented to calculate the change in position of the neutral axis numerically, accounting for the material non-linearity. It is shown that for the range of parameters examined in the present work, the error introduced by neglecting the translation of the neutral axis is small. Thus, Eq. 11 provides a good approximation of the neutral axis position and is computationally significantly less costly.

For the range of material and specimen parameters examined in Section 5, the error of the J integral method is below 15% in most cases (for $\hat{\sigma}/\sigma_u < 1$). The variation of the experimentally measured fracture resistance values is usually much higher than 15%, see for example the experimental results of Sørensen and Jacobsen [16] and De Souza et al. [36]. Thus, it can be argued that the error of the proposed J integral method is so small that it allows the method to be used with confidence in practise.

6.2. Implication for experiments

The steady-state fracture resistance values, J_{ss}, (Section 5) were taken from the part of the curve of Fig. 9 where there is a plateau in the J integral. This corresponds to openings larger than the critical opening for complete

failure ($\delta^*/\delta_c = 1$). If there was no toughening due to plasticity, J_{ss} would be reached for $\delta^* = \delta_c$.

It is possible to monitor the end-opening during loading using a camera, an optical microscope or by performing the experiment inside the chamber of an Environmental Scanning Electron Microscope (ESEM) [36]. In this case, it is possible to identify the critical opening for complete failure δ_c experimentally. The corresponding J value will then be close to J_c since the amount of unloading will be small. In the cohesive law determination, Eq. 1, only data up to δ_c should be used. Consequently, the cohesive law parameters could be extracted more accurately.

As mentioned in Section 5, the noise in the computed cohesive laws (see Figs. 10 and 12) is an artifact related to the differentiation method used (Eq. 28) and the number of increments of the finite element solution. In practice the experimental data, J *vs* δ^*, can be fitted with polynomial functions *e.g.* splines or Chebyshev polynomials [29]. With the use of polynomials or other differentiable functions [37], smooth cohesive laws can be extracted.

The parameter study in the present paper covers many realistic engineering materials. If the linear elastic material is steel ($E^{\#1}$=200 GPa), then the curve $E^{\#2}/E^{\#1}$=0.01 corresponds to non-linear materials such as polymers ($E^{\#2} \sim$ 2-4 GPa), whereas for $E^{\#2}/E^{\#1} = 0.1$ the non-linear material can represent *e.g.* fibre reinforced composite materials ($E^{\#2} \sim$ 20-40 GPa).

7. Summary and Conclusions

A test procedure for extracting mode I cohesive laws (peak traction, critical openings and shape) for materials with non-linear stress-strain behaviour is developed. The method uses a J integral specimen (Double Cantilever Beam sandwich specimen loaded with pure bending moments) subjected to monotonically increasing moments. The requirement that there is no unloading at any material point is not strictly fulfilled in a small region at the wake of the crack tip, but the beams of the DCB specimen does not unload macroscopically during crack opening and crack propagation. It is shown that the difference between the steady-state fracture resistance, J_{ss}, and J_c is below 16% in the range of material and specimen parameters examined. This is smaller than the usual scatter in experimental fracture resistance data. Thus, it can be concluded that the method can be used in practise for cohesive law determination of materials undergoing large-scale yielding.

Acknowledgement

BFS was supported by the Danish Centre for Composite Structures and Materials for Wind Turbines (DCCSM), Grant No. 09-067212 from the Danish Council for Strategic Research. The idea for extending the J integral testing approach of DCB specimens loaded with moments to large scale yielding problems came in discussions with Dr. Rasmus C. Østergaard.

Appendix A. Neutral axis change in position with plasticity

In Sub-section 3.1, it was assumed that the neutral axis does not change position as plasticity develops in the beams of the material #2. With this assumption, the neutral axis position is given by Eq. 11. In this Appendix, the neutral axis position is calculated analytically, accounting for the non-linear stress-strain law of material #2 in order to assess the accuracy of Eq. 11.

Since the specimen is symmetric, the analysis is restricted to one of the bimaterial beams. If we consider the upper-half of the DCB specimen (see Fig. 5), the axial force in the beam-end, N, is given by (plane stress):

$$\frac{N}{B} = \int_{\Delta-H-h}^{\Delta-H} \sigma_{11}^{\#2}(y)dy + \int_{\Delta-H}^{\Delta} \sigma_{11}^{\#1}(y)dy \tag{A-1}$$

where $\sigma_{11}^{\#2}$ is given in Eq. 3 and $\sigma_{11}^{\#1} = E^{\#1}\epsilon_{11}$ (see Eq. 22). Since the beam ends are subjected to pure bending moments, the axial force, N, is equal to zero. Using Eq. 9 and performing the integration, we obtain:

$$\begin{aligned}\frac{N}{B} &= \frac{E^{\#2}\hat{\epsilon}}{2\Delta}\Big(2\Delta h - h^2 - 2Hh\Big) - \frac{\sigma_o\hat{\epsilon}^2}{3\Delta^2}\Big((\Delta - H)^3 \\ &\quad -(\Delta - H - h)^3\Big) + \frac{E^{\#1}\hat{\epsilon}}{2\Delta}H(2\Delta - H) = 0\end{aligned} \tag{A-2}$$

Eq. A-2 is a second order equation in $\hat{\epsilon}$ which together with Eq. 14 form a system of two second order equations with two unknowns $\hat{\epsilon}$ and Δ. This system can be solved numerically giving Δ as a function of M using Mathematica [38].

Fig. A.1 shows the change in position of the neutral axis for six different ratios of $\hat{\sigma}/\sigma_u$ as a function of the applied moment for values of M up to

the point of steady-state for each $\hat{\sigma}/\sigma_u$ ratio. At steady-state, the neutral axis has moved by 0.17% for $\hat{\sigma}/\sigma_u$=0.35, whereas for $\hat{\sigma}/\sigma_u$=1.0, the change in position is 0.33%.

Next in Fig. A.2, the change of the neutral axis position is examined as a function of the Young's modulus of the non-linear material for $\hat{\sigma}/\sigma_u$=0.9. The change in position is less than 1.5 % for $E^{\#2}/E^{\#1}$ =0.1. For this case the corresponding difference in the steady-state fracture resistance is 0.45%. Thus, the change in position is relatively small.

Appendix B. Examples of closed form solutions for homogeneous DCB specimens

For a homogeneous (*i.e.* consisted of one material only) DCB specimen loaded with pure bending moments it is possible for certain case to obtain the J integral equation in closed form when the material is not linear elastic. The closed form J integral solutions are given below for two non-linear material laws: a power law and an elastic-ideal plastic law, shown schematically in Fig. B.1.

Appendix B.1. Power law stress-strain behaviour

If the stress-strain behaviour of the non-linear material can be described by a power law constitutive equation:

$$\sigma_{11} = f(\epsilon_{11}) = \sigma_o \epsilon_{11}^n \tag{B-1}$$

where σ_o is a constant and n is a strain-hardening exponent, then Eq. 14 can be solved analytically for $\hat{\epsilon}$:

$$\hat{\epsilon} = \sqrt[n]{2(n+2)\frac{M}{\sigma_o B h^2}} \tag{B-2}$$

and the strain energy density function, Φ is given by:

$$\Phi = \int_0^{\epsilon_{11}} \sigma_o \epsilon_{11}^n d\epsilon_{11} = \frac{1}{n+1}\sigma_o \epsilon_{11}^{n+1} \tag{B-3}$$

With Eqs. B-1, B-2 and B-3, J_5 (Eq. 24) can be obtained in closed form, and through Eq. 25, the J integral along the external boundaries of the specimen is given by:

$$J_{ext} = \frac{4n}{n+1}\frac{M}{Bh}\Big[2(n+2)\frac{M}{\sigma_o B h^2}\Big]^{1/n} \tag{B-4}$$

where h is the thickness of each beam (the total thickness of the DCB specimen is $2h$). Eq. B-4 is identical to the I integral solution of Thouless et al. [27].

Appendix B.2. Elastic-ideal plastic stress-strain behaviour

For an elastic-ideal plastic material having a Young's modulus E and a yield stress σ_u (see Fig. B.1), the stress-strain relationship is:

$$\sigma_{11} = \begin{cases} E\epsilon_{11}, & \text{for } 0 < |\epsilon_{11}| \leq \dfrac{\sigma_u}{E}, \\ \sigma_u, & \text{for } |\epsilon_{11}| > \dfrac{\sigma_u}{E}, \end{cases} \tag{B-5}$$

It can be shown that the strain energy density function (under uniaxial tension), Φ, is given by:

$$\Phi = \sigma_u\Big(\epsilon_{11} - \frac{1}{2}\frac{\sigma_u}{E}\Big) \tag{B-6}$$

Following a similar procedure as above (Section Appendix B.1), it can be shown that the J integral along the external boundaries of the DCB specimen is given by:

$$J_{ext} = \frac{\sigma_u^2 h}{2E}\left[1 - \frac{4}{3}\frac{\tilde{h}}{h}\right] = \frac{\sigma_u^2 h}{2E}\left[1 - \frac{2}{3}\sqrt{3 - \frac{48M}{\sigma_u B h^2}} \quad \right] \tag{B-7}$$

where the ratio $\tilde{h}/h$ describes the region of large scale plasticity (see Fig. B.2).

The beams become fully plastic ($\tilde{h} = h/2$), when:

$$M = \frac{\sigma_u B h^2}{24}. \tag{B-8}$$

Then, Eq. B-7 becomes:

$$J_{ext} = \frac{\sigma_u^2 h}{6E}. \tag{B-9}$$

This is the maximum J integral value of the specimen. If the work of separation per unit area J_c exceeds this value, the specimen will yield but

not fracture. Fracture can be obtained for specimens having larger beam height, *i.e.* by increasing h.

References

[1] Kaninen MF, Popelar CH. Advanced fracture mechanics. New York: Oxford University Press; 1985.

[2] Dugdale DS. Yielding of steel sheets containing slits. Journal of the Mechanics and Physics of Solids 1960;8:100–4.

[3] Barenblatt GI. The mathematical theory of equilibrium cracks in brittle fracture. Advances in Applied Mechanics 1962;77:55–129.

[4] Foote RML, Mai YW, Cotterell B. Crack growth resistance curves in strain-softening materials. Journal of the Mechanics and Physics of Solids 1986;34:593–607.

[5] Hillerborg A. Application of the fictitious crack model to different types of materials. International Journal of Fracture 1991;51:95–102.

[6] Cox BN, Marshall DB. The determination of crack bridging forces. International Journal of Fracture 1991;49:159–76.

[7] Suo Z, Bao G, Fan B. Delamination R-curve phenomena due to damage. Journal of the Mechanics and Physics of Solids 1992;40:1–16.

[8] Needleman A. A continuum model for void nucleation by inclusion debonding. Journal of Applied Mechanics 1987;54(3):525–31.

[9] Tvergaard V, Hutchinson JW. The relation between crack growth resistance and fracture process parameters in elastic plastic solids. Journal of the Mechanics and Physics of Solids 1992;40:1377–97.

[10] Yang QD, Thouless MD, Ward SM. Numerical simulations of adhesively-bonded beams failing with extensive plastic deformation. Journal of the Mechanics and Physics of Solids 1999;47(6):1337–53.

[11] Mohammed I, Liechti KM. Cohesive zone modeling of crack nucleation at bimaterial corners. Journal of the Mechanics and Physics of Solids 2000;48:735–64.

[12] Kafkalidis MS, Thouless MD. The effects of geometry and material properties on the fracture of single lap-shear joints. Internatonal Journal of Solids and Structures 2002;39:4367–83.

[13] Zhang Z, Paulino GH. Cohesive zone modelling of dynamic failure in homogeneous and functionally graded materials. International Journal of Plasticity 2005;21(6):1195–254.

[14] Van den Bosch MJ, Schreurs PJG, Geers MGD. An improved description of the exponential Xu and Needleman cohesive zone law for mixed mode decohesion. Engineering Fracture Mechanics 2006;73:1220–34.

[15] Sørensen BF, Gamstedt EK, Østergaard RC, Goutianos S. Micromechanical model of cross-over fibre bridging - prediction of mixed mode bridging laws. Mech Mater 2008;40:220–34.

[16] Sørensen BF, Jacobsen TK. Determination of cohesive laws by the J integral approach. Engineering Fracture Mechanics 2003;70(14):1841–58.

[17] Yang QD, Thouless MD. Mixed-mode fracture analyses of plastically-deforming adhesive joints. International Journal of Fracture 2001;110:175–87.

[18] Cotterell B, Mai YW. Fracture mechanics of cementitious materials. Blackie Academic & Professional, an Imprint of Chapman and Hall; 1996.

[19] Brenet P, Conchin F, Fantozzo G, Reynaud P, Rouby D, Tallaron C. Direct measurement of the crack bridging tractions: a new approach of the fracture behavior of ceramic-matrix composites. Composites Science and Technology 1996;56:817–23.

[20] Rice JR. A path independent integral and the approximate analysis of strain concentrations by notches and cracks. Journal of Applied Mechanics 1968;35:379–86.

[21] Li VC, Ward RJ. A novel testing technique for post-peak tensile behaviour of cementitious materials. In: Mihashi H, Takahashi H, Wittmann FH, editors. Fracture toughness and fracture energy-testing

methods for concrete and rocks. Rotterdam: A. A. Balkema Publishers; 1989, p. 183–95.

[22] Bao G, Suo Z. Remarks on crack-bridging concepts. Applied Mechanics Reviews 1992;45:355–61.

[23] Sørensen BF, Jacobsen TK. Large-scale bridging in composites: R-curves and bridging laws. Composites Part A - Applied Science and Technology 1998;29:1443–51.

[24] Bao G, Ho S, Suo Z. The role of material orthotropy in fracture specimens for composites. International Journal of Solids and Structures 1992;29(9):1105–16.

[25] Budiansky B. A reassessment of deformation theories of plasticity. Journal of Applied Mechanics 1959;81:259–64.

[26] Lundsgaard-Larsen C, Sørensen BF, Berggreen C, Østergaard RC. A modified dcb sandwich specimen for measuring mixed-mode cohesive laws. Engineering Fracture Mechanics 2008;75:2514–30.

[27] Thouless MD, Kafkalidis MS, Ward SM, Bankowski Y. Toughness of plastically-deforming asymmetric joints. Scripta Materialia 1997;37:1081–7.

[28] Hutchinson JW. On steady quasi-static crack growth. Tech. Rep.; Harvard University; 1974.

[29] Sørensen BF, Kirkegaard P. Determination of mixed mode cohesive laws. Engineering Fracture Mechanics 2006;73:2642–61.

[30] Goutianos S, Arévalo R, Sørensen BF, Peijs T. Effect of processing conditions on fracture rresistance and cohesive laws of binderfree all-cellulose composites. Applied Composite Materials 2014;21:805–25.

[31] Abaqus Version 6.11 . Abaqus Inc; 2012.

[32] Turon A, Davila CG, Camanho PP, Costa J. An engineering solution for mesh size effects in the simulation of delamination using cohesive zone models. Engineering Fracture Mechanics 2007;74:1665–82.

[33] Tvergaard V, Hutchinson JW. Toughness of an interface along a thin ductile layer joining elastic solids. Philosophical Magazine A 1994;70:641–56.

[34] Hutchinson JW. Fundamentals of the phenomenological theory of nonlinear fracture mechanics. Journal of Applied Mechanics 1983;50:1042–51.

[35] Budiansky B, Hutchinson JW, Lambropoulos JC. Strength characteristics of transformation-toughened zirconia. International Journal of Solids and Structures 1983;19(4):337–55.

[36] De Souza JA, Goutianos S, Skovgaard M, Sørensen BF. Fracture resistance curves and toughening mechanisms in polymer based dental composites. Journal of the Mechanical Behavior of Biomedical Materials 2011;4(4):558–71.

[37] Lindhagen JE, Berglund LA. Application of bridging-law concepts to short-fibre composites - Part 1: DCB test procedures for bridging law and fracture energy. Composites Science and Technology 2000;60:871–83.

[38] Wolfram Research, Inc . Mathematica Edition: Version 7.0. Champaign, Illinois: Wolfram Research, Inc; 2008.

Figure Captions

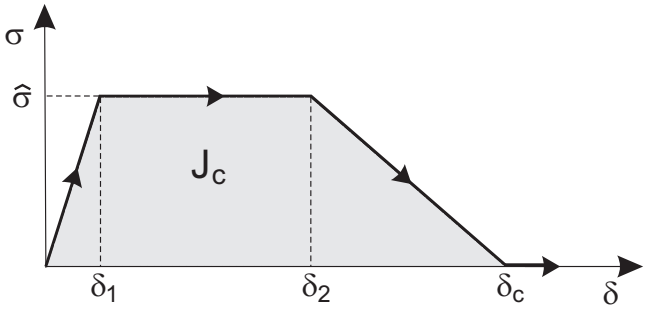

Figure 1: Schematic illustration of the idealised cohesive law used in this study. J_c is the mode I work of separation, δ_c, the critical separation, the opening at complete failure, and $\hat{\sigma}$ is the peak traction.

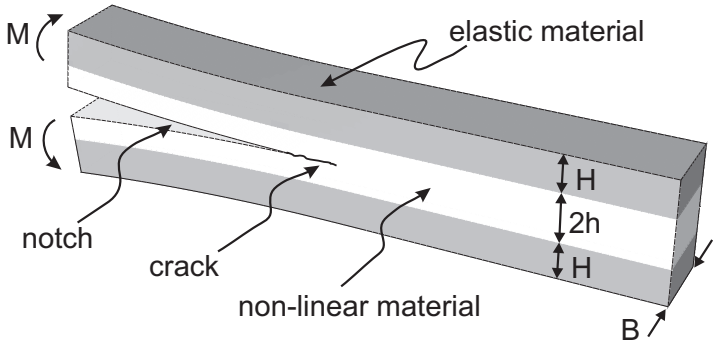

Figure 2: Double Cantilever Beam (DCB) sandwich specimen loaded with pure bending moments.

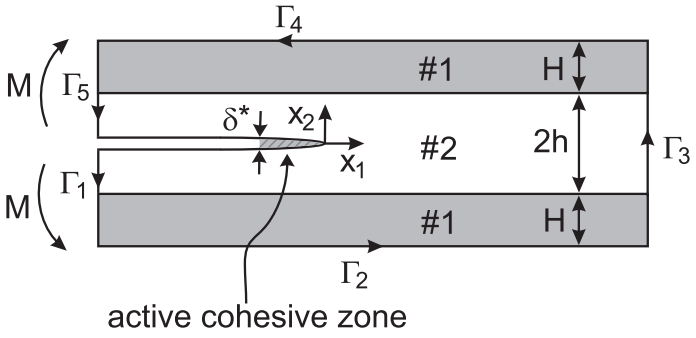

Figure 3: Two-dimensional specimen representation and J integral path Γ_i with $i = 1, 5$ along the external boundaries. #1: elastic material, #2 non-linear elastic material.

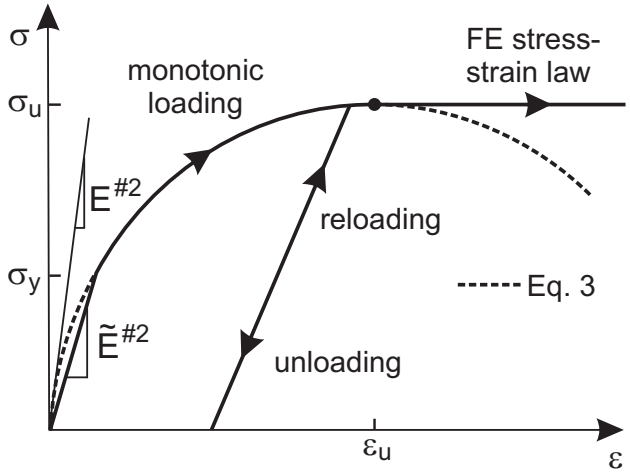

Figure 4: Stress-strain behaviour described by a monotonically increasing function f as long there is no unloading. The material can be *e.g.* elastic-plastic.

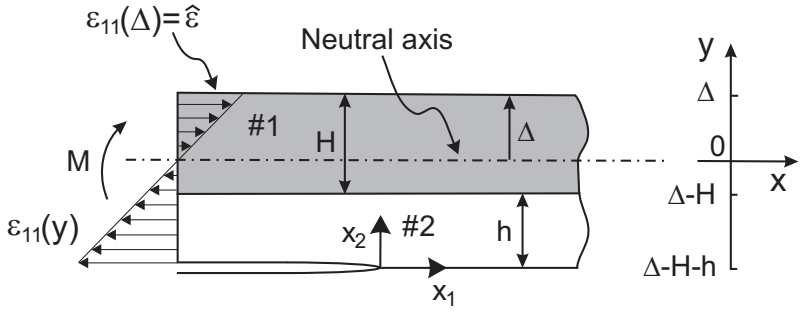

Figure 5: Definition of a local coordinate system $(x - y)$ with origin the position of the neutral axis (only half of the specimen, $x_2 > 0$, of Fig. 3 is considered).

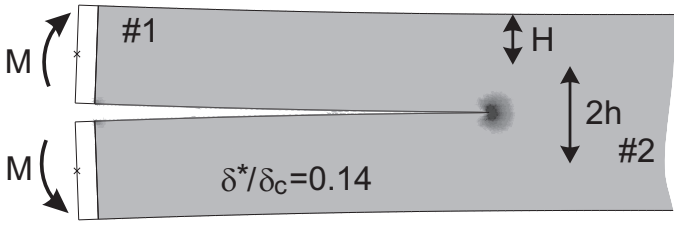

(a)

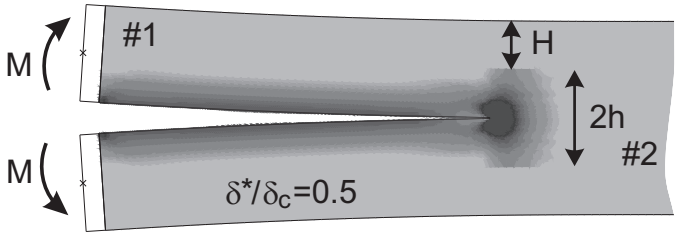

(b)

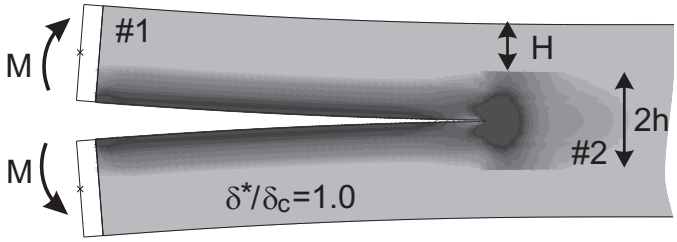

(c)

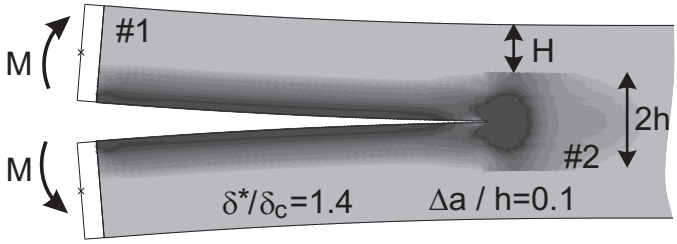

(d)

Figure 6: Equivalent plastic strain contours as a function of the end-opening, δ^* for $\hat{\sigma}/\sigma_u = 1$, $E^{\#2}/E^{\#1} = 0.02$ and $E^{\#2}/\sigma_o = 0.1$ (see Fig. 16): a) $J/J_c = 0.25$, b) $J/J_c = 0.80$, c) $J/J_c = 1.13$, and d) $J/J_c = 1.16$.

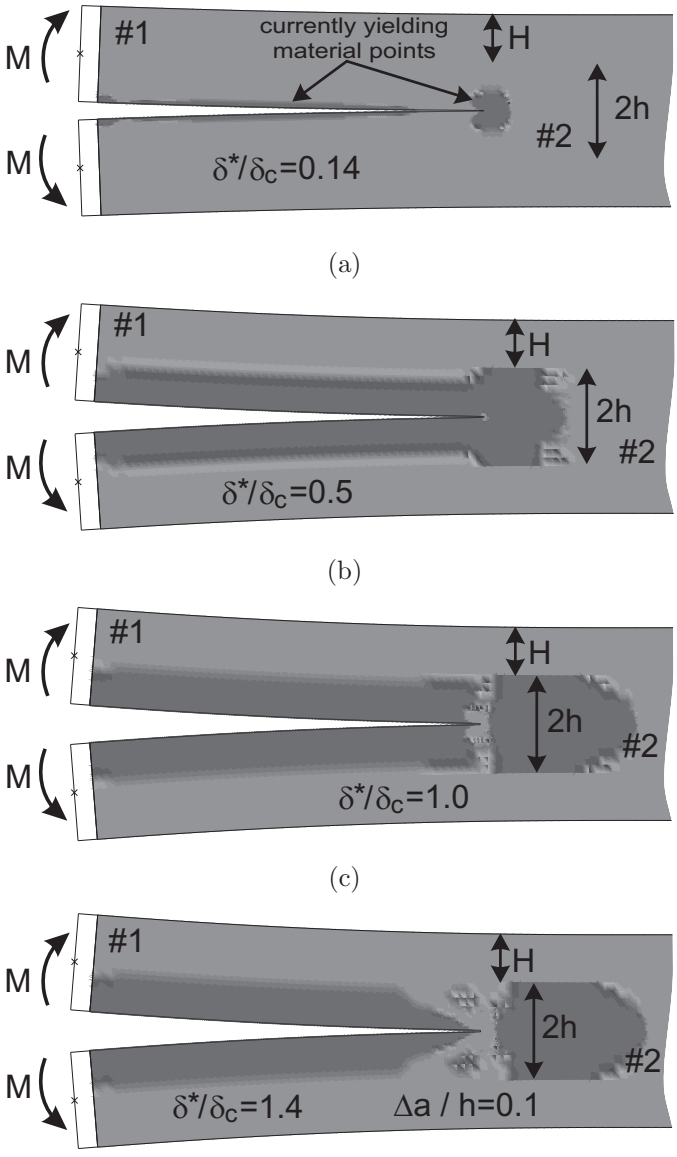

Figure 7: Active plastic zone contours as a function of the end-opening, δ^* for $\hat{\sigma}/\sigma_u = 1$, $E^{\#2}/E^{\#1} = 0.02$ and $E^{\#2}/\sigma_o = 0.1$ (see Fig. 16): a) $J/J_c = 0.25$, b) $J/J_c = 0.80$, c) $J/J_c = 1.13$, and d) $J/J_c = 1.16$.

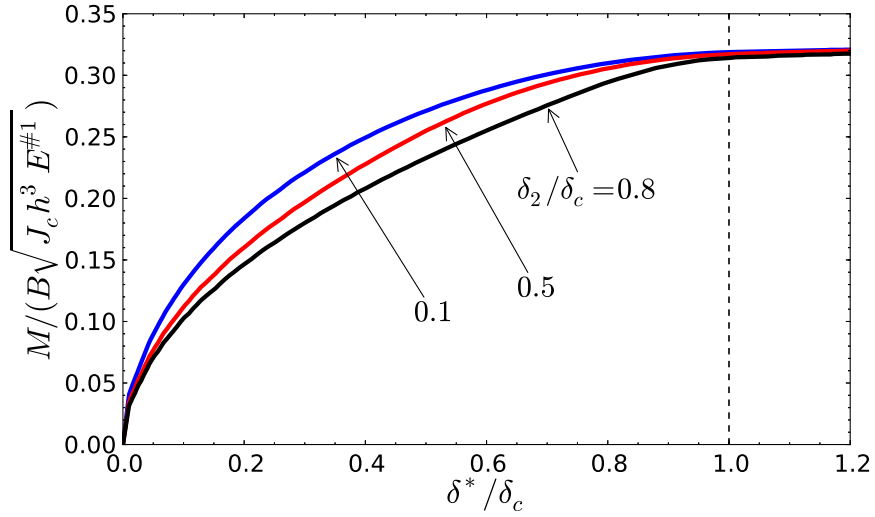

Figure 8: Extracted, M, *versus* end-opening, δ^*, with both variables extracted from the FE model ($h/H = 1$, $\delta_1/h = 2 \times 10^{-4}$, $\delta_c/h = 2 \times 10^{-2}$, $\hat{\sigma}/\sigma_u = 0.75$, $\sigma_y/E^{\#2} = 0.01$, $E^{\#2}/\sigma_o = 0.2$, and $E^{\#2}/E^{\#1} = 0.01$).

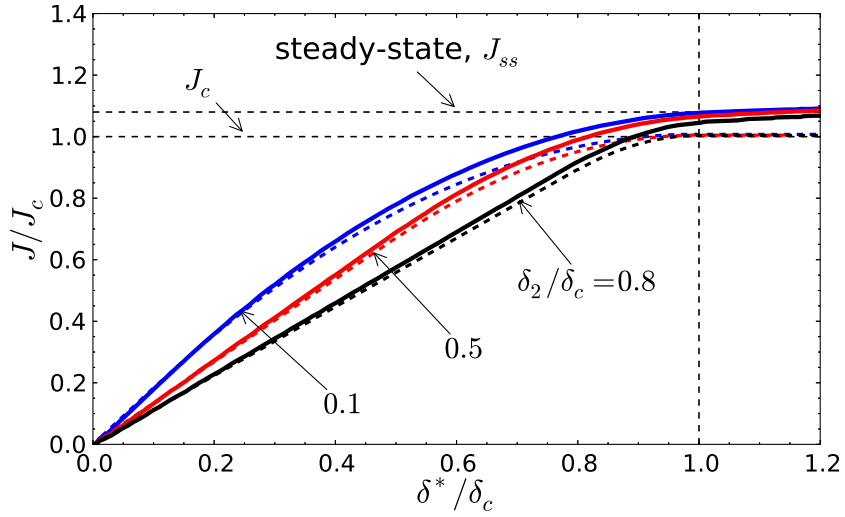

Figure 9: J *versus* δ^* where J is computed from M (Fig. 8) using the analytical method of Section 3. The dotted lines represent the theoretical fracture resistance curves, Eq. 27.

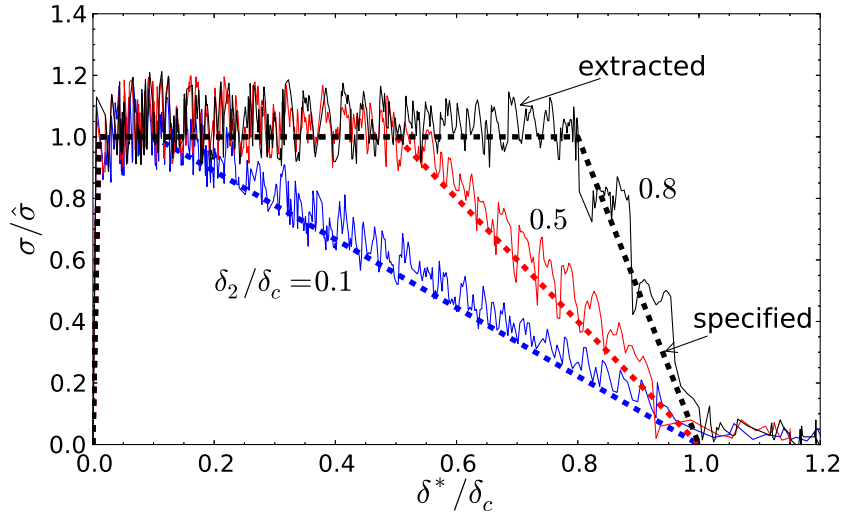

Figure 10: Extracted cohesive laws from J and δ^* (Fig. 9) using Eq. 28 (solid lines). The dashed lines represent the cohesive laws specified as input in the finite element model.

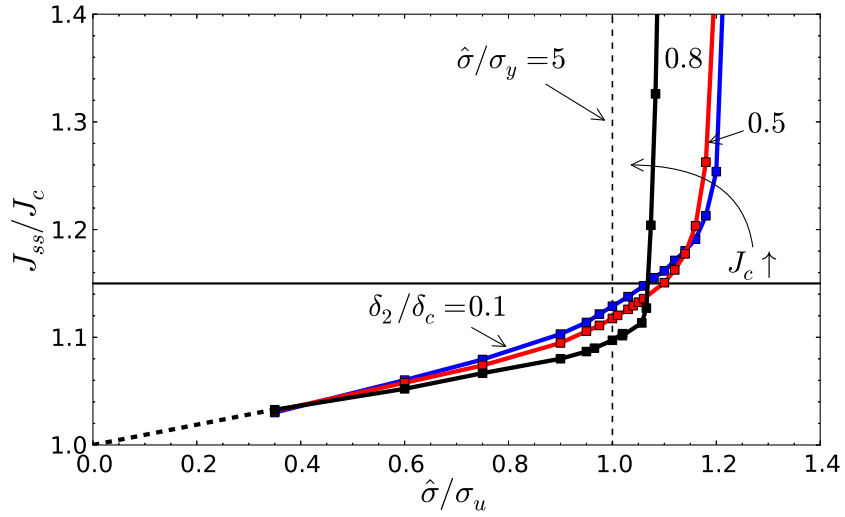

Figure 11: Steady-state fracture resistance as a function of the cohesive peak stress, $\hat{\sigma}$, for three δ_2/δ_c ratios ($h/H = 1$, $\delta_c/h = 2 \times 10^{-2}$, $\sigma_y/E^{\#2} = 0.01$, $E^{\#2}/\sigma_o = 0.2$, and $E^{\#2}/E^{\#1} = 0.01$).

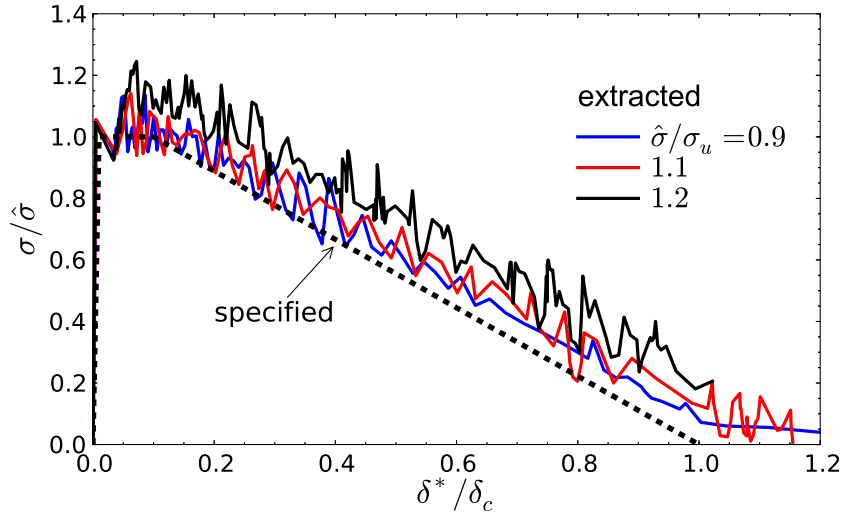

Figure 12: Extracted cohesive laws using Eq. 28 (solid lines) for $\delta_2/\delta_c = 0.1$ (see Fig. 11). The dashed line represent the cohesive law specified as input in the finite element model.

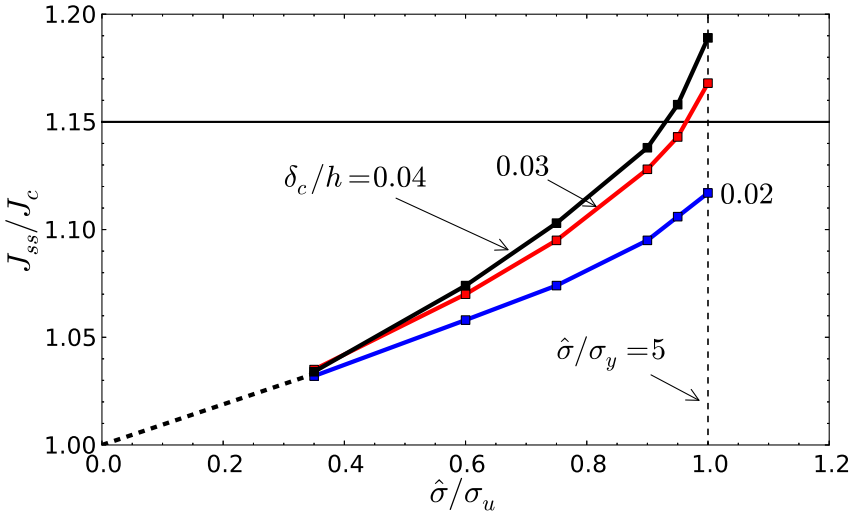

Figure 13: Steady-state fracture resistance as a function of the cohesive peak stress, $\hat{\sigma}$, for three δ_c/h ratios ($h/H = 1$, $\delta_2/h = 0.01$, $\sigma_u/E^{\#2} = 0.05$, $E^{\#2}/\sigma_o = 0.2$, and $E^{\#2}/E^{\#1} = 0.01$).

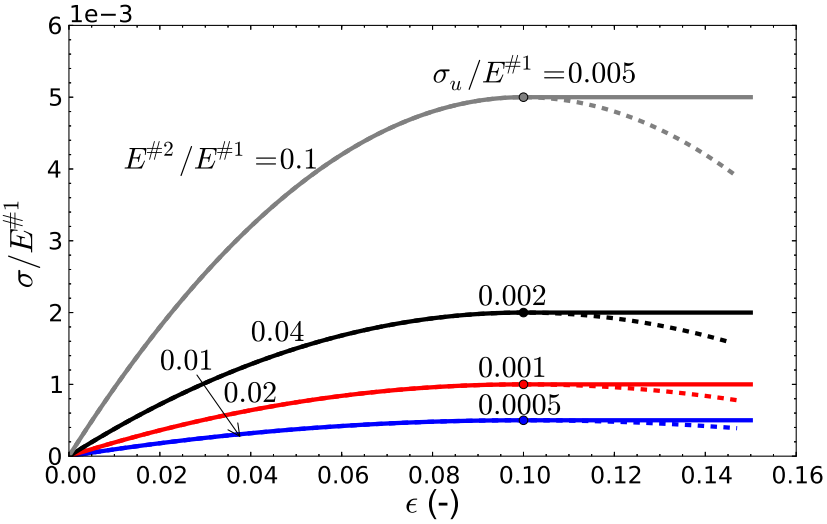

Figure 14: Normalised stress-strain curves, Eq. 3, for the non-linear test material (material #2) with different $E^{\#2}$ values. The ratio $E^{\#2}/\sigma_o$ is constant, $E^{\#2}/\sigma_o = 0.2$.

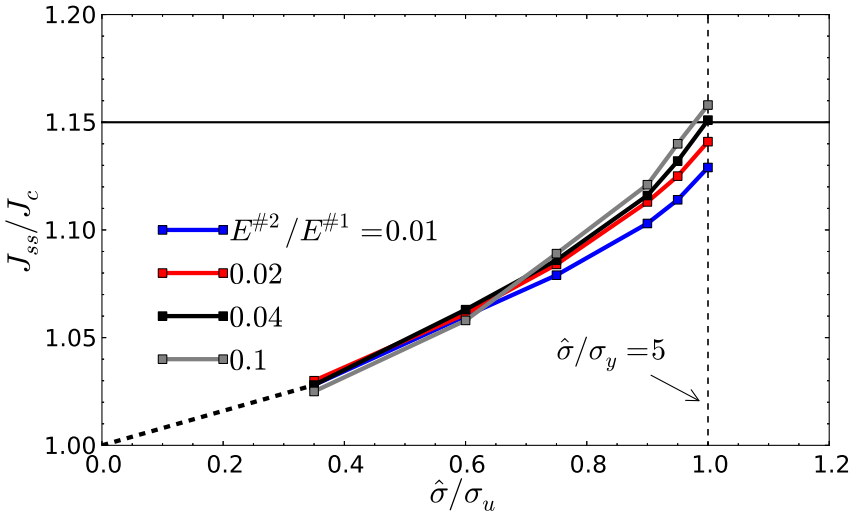

Figure 15: Normalised steady-state fracture resistance as a function of the cohesive peak stress, $\hat{\sigma}$ for four $E^{\#2}/E^{\#1}$ ratios ($h/H = 1$, $\delta_1/h = 2 \times 10^{-4}$, $\delta_2/h = 2 \times 10^{-2}1$, $\delta_c/h = 0.02$, $\sigma_u/E^{\#2} = 0.05$, and $E^{\#2}/\sigma_o = 0.2$).

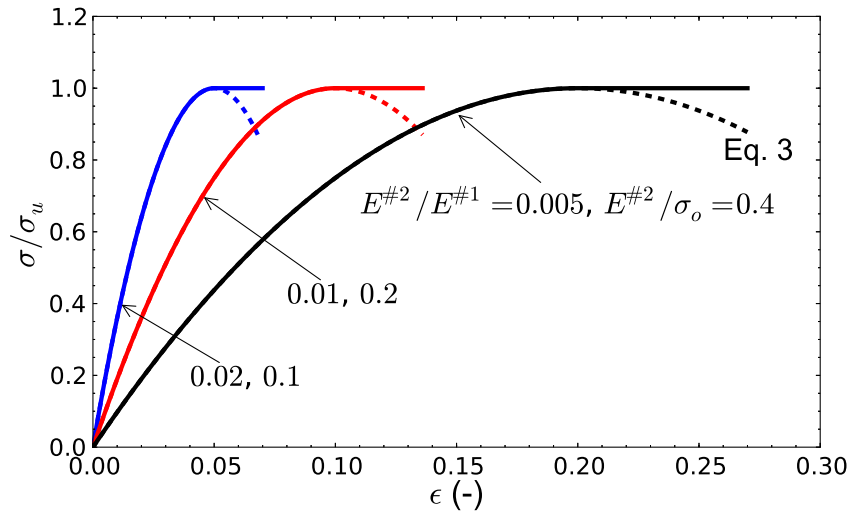

Figure 16: Normalised stress-strain curves, Eq. 3, for the non-linear test material (material #2) with different σ_o and $E^{\#2}$ values to keep σ_u constant.

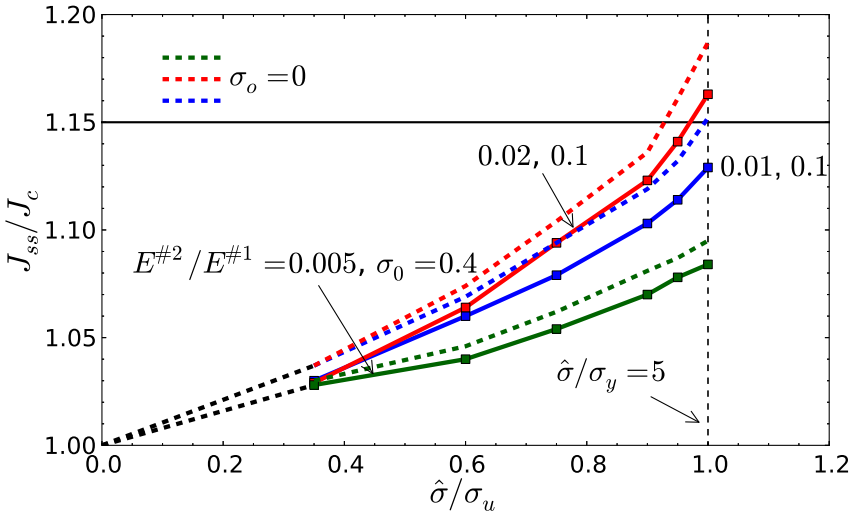

Figure 17: Normalised steady-state fracture resistance as a function of the cohesive peak stress, $\hat{\sigma}$, for the three different stress-strain curves of Fig. 16 ($h/H = 1$, $\delta_1/h = 2 \times 10^{-4}$, $\delta_2/\delta_c = 0.1$, $\delta_c/h = 2 \times 10^{-1}$).

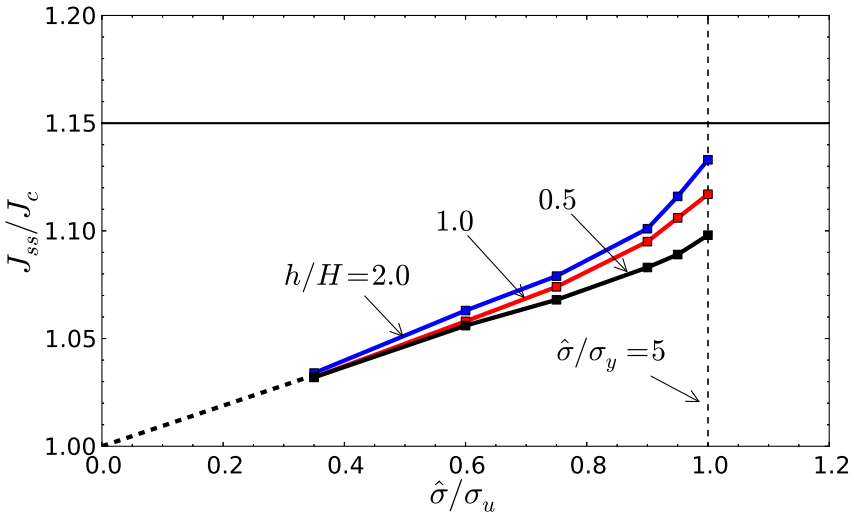

Figure 18: Normalised steady-state fracture resistance as a function of the cohesive peak stress, $\hat{\sigma}$, for different h/H ratios ($\delta_1/h = 2 \times 10^{-4}$, $\delta_2/h = 2 \times 10^{-3}$, $\delta_c/h = 2 \times 10^{-1}$, $\sigma_u/E^{\#1} = 0.05$, $E^{\#2}/E^{\#1} = 0.01$, and $E^{\#2}/\sigma_o = 0.2$).

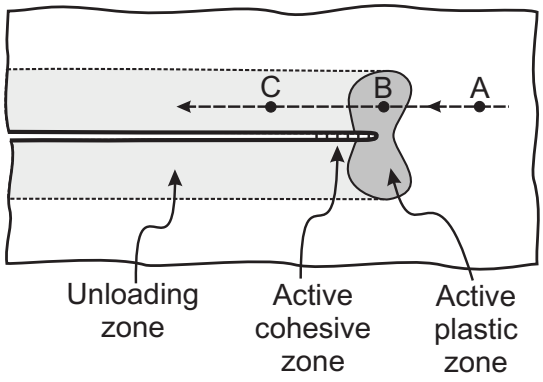

(a)

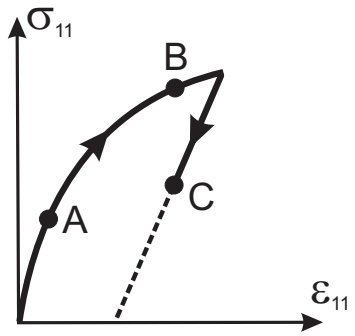

(b)

Figure 19: Illustration of the history of stress as a point approaching and moving past the active, fully developed cohesive zone under steady-state cracking. (a) Schematics of the point relative to the active cohesive zone: (A) ahead of the active plastic zone, (B) within the active plastic zone and (c) behind the active plastic zone, (b) the associated loading- and unloading history.

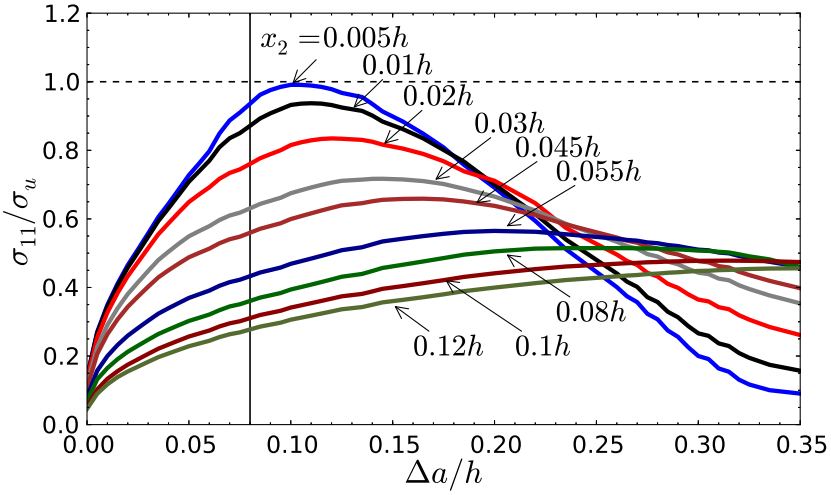

Figure 20: Stress component σ_{11} in material points in material #2 located at $x_1 = 0.08h$ and different x_2 values, see Fig. 19. The solid line represents the x_1 coordinate of the material points relative to the initial notch.

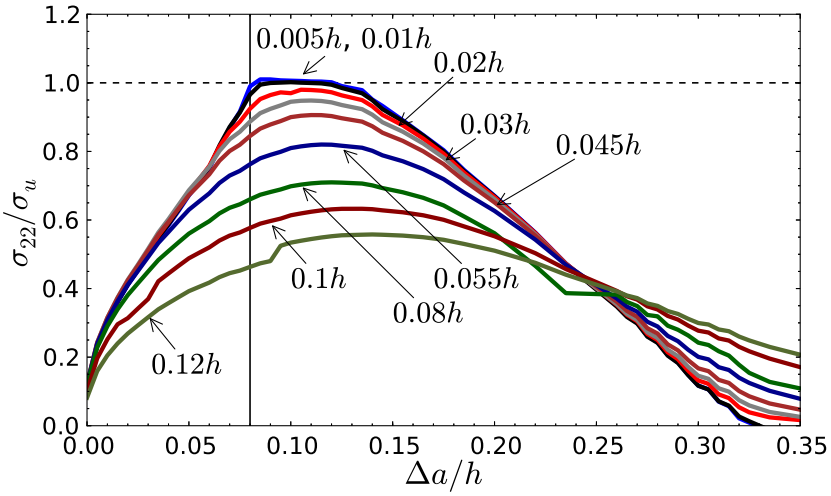

Figure 21: Stress component σ_{22} in material points in material #2 located at $x_1 = 0.08h$ and different x_2 values, see Fig. 19. The solid line represents the x_1 coordinate of the material points relative to the initial notch.

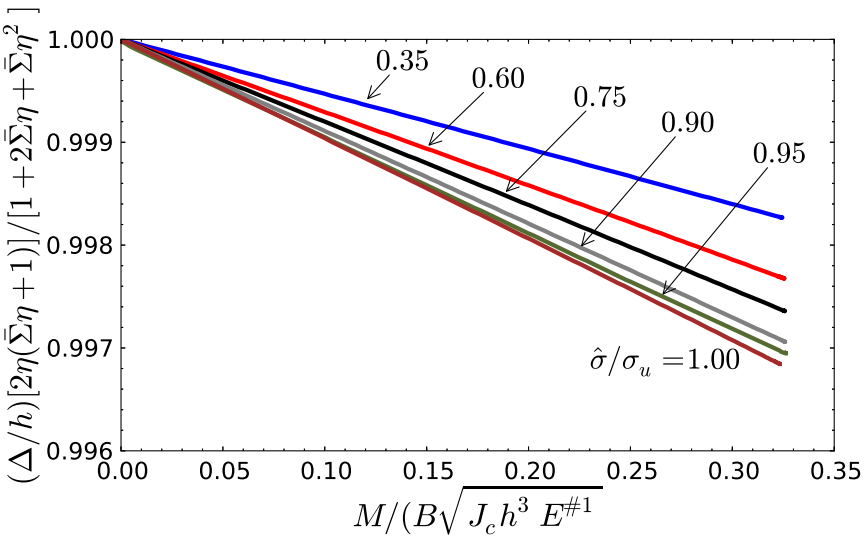

Figure A.1: Neutral axis position as a function of applied moment, M, for six different ratios of $\hat{\sigma}/\sigma_u$. $E^{\#2}/E^{\#1}$=0.02 and $E^{\#2}/\sigma_o = 0.1$ (see Fig. 17).

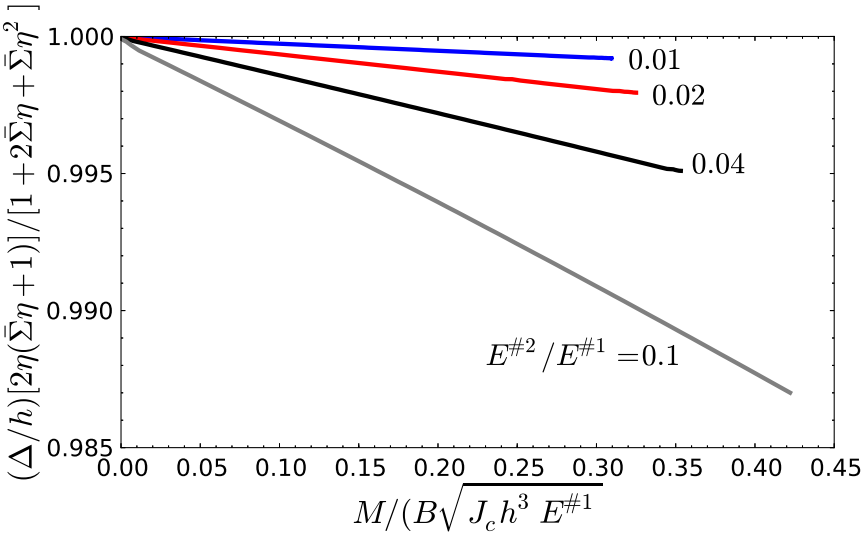

Figure A.2: Neutral axis position as a function of applied moment, M, for four different of $E^{\#2}/E^{\#1}$. $\hat{\sigma}/\sigma_u$=0.9 (see Fig. 15).

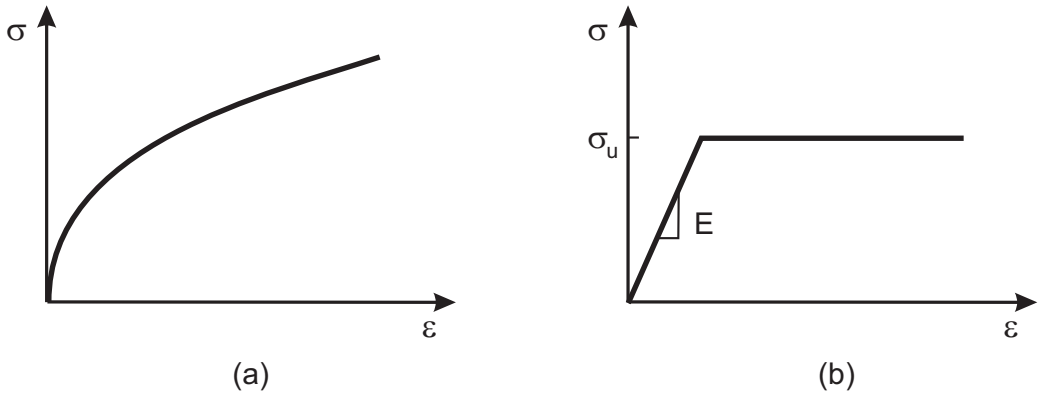

Figure B.1: a) power law, and b) elastic-ideal plastic law.

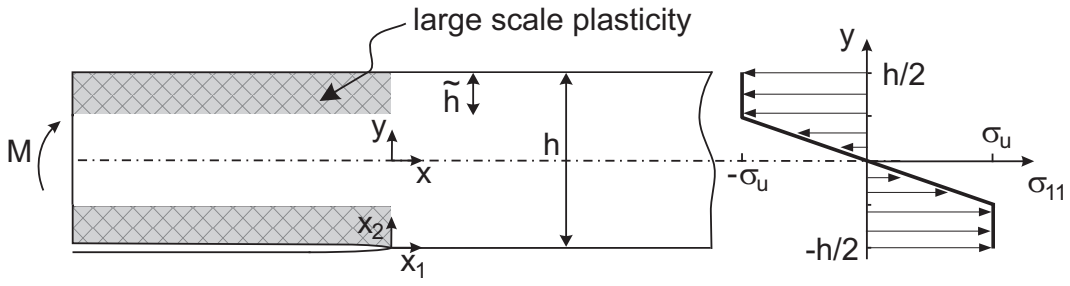

Figure B.2: DCB specimen loaded with pure bending moments for an elastic-perfectly plastic material (Due to symmetry only half of the specimen is shown).